DOI: 10.13009/EUCASS2023-606
Aerospace Europe Conference 2023 – 10TH EUCASS – 9TH CEAS

Modeling of swirl injection effects in a H2O2-HDPE hybrid rocket

Marco Fabiani[⋆†], *Mario Tindaro Migliorino*[⋆], *Daniele Bianchi*[⋆], *Francesco Nasuti*[⋆],
Massimo Franco[⋆⋆], *Francesco Barato*[⋆⋆⋆], *Nicolas Bellomo*[⋆⋆], *Daniele Pavarin*[⋆⋆]
[⋆]*Sapienza University of Rome*
00184 Rome, Italy
m.fabiani@uniroma1.it · mariotindaro.migliorino@uniroma1.it · daniele.bianchi@uniroma1.it · francesco.nasuti@uniroma1.it
[⋆⋆]*Technology for Propulsion and Innovation Srl (T4i)*
35121 Padua, Italy
m.franco@t4innovation.com · n.bellomo@t4innovation.com · d.pavarin@t4innovation.com
[⋆⋆⋆] *University of Padua*
35121 Padua, Italy
francesco.barato@unipd.it
[†]Corresponding author

Abstract

The flow features and performance parameters of a swirl-injected hybrid rocket burning H_2O_2 and HDPE are numerically investigated by means of axisymmetric Reynolds-averaged Navier-Stokes simulations. Several firing tests of a 300 N hybrid rocket are rebuilt, with satisfactory results for both the average regression rate and the chamber pressure, confirming how the adopted numerical approach can be successfully employed in the design of hybrid rockets. The dynamics of the swirling flow are studied, analyzing the strong decay of the swirling motion along the engine, and the effect of swirl intensity on the fuel regression rate and the propellant mixing process.

1. Introduction

Hybrid rocket engines (HREs) are rocket propulsion devices burning a solid fuel and a liquid/gaseous oxidizer, which aim at combining the simplicity of solid rocket motors with the restarting and throttling capabilities of liquid rocket engines, while having an increased safety thanks to the different phases in which the propellants are stored [1, 2]. The fuel grain regression and the propellant mixing processes are entailed by the complex flowfield which develops in the combustion chamber, and for this reason computational fluid dynamics (CFD) analysis can aid HREs modeling and design, reducing the number of needed firing tests and providing insights on the physical phenomena taking place inside the engine.

Typical HREs fuels are pyrolizing polymers, such as high density polyethylene (HDPE), which are usually characterized by low values of the fuel regression rate, which in turn limits the amount of thrust reachable with a given engine size [3]. For this reason, and also to improve combustion efficiency and stability, swirl injection is often employed, injecting the oxidizer at an angle with respect to the motor axis [4]. In fact, the larger velocity (for the same mass flow rate) leads to an increase in convective heat flux and mixing [5, 6, 7, 8, 9, 10]. In swirl-injected HREs an additional design parameter has to be considered, namely the rotational motion intensity, which is quantified by the swirl number (SN) [4], defined as the ratio between the flux of angular momentum and the flux of axial momentum

$$SN = \frac{\text{angular momentum flux}}{r_{\text{wall}} \times \text{axial momentum flux}} = \frac{\int_S (\rho u w r) dS}{r_{\text{wall}} \int_s (\rho u^2) dS} \tag{1}$$

where r_{wall} is the wall radius (needed to make SN a dimensionless quantity), ρ the fluid density, u and w the axial and tangential velocity, and S is the cross-section. The swirl number decays along the engine, due to friction [11], addition of mass and energy [12], and change in cross-section [4]. Both the swirl number and its decay can be evaluated through reduced-order models, CFD analysis, and/or flow experimental measurements. However, SN is not convenient for a-priori design purposes, being dependent on the flow distribution and evolution of a specific test case. For this reason it is useful to introduce the geometric swirl number (SN_g), which is an approximation of the value attained by the swirl

DOI: 10.13009/EUCASS2023-606

intensity SN considering only the oxidizer, and neglecting any dissipation or viscous contribution [13, 14]. Under these hypotheses, SN_g can be computed by the following equation

$$SN_g = \frac{\pi \left(r_{\text{wall}} - r_h\right) r_{\text{wall}}}{n_h \pi r_h^2} \tag{2}$$

which is a function of sole geometric quantities (the wall radius r_{wall}, the injector hole radius r_h, and the number of injector holes n_h), and can thus be readily employed.

In this work, a numerical approach based on axisymmetric Reynolds-averaged Navier-Stokes simulations, with submodels accounting for turbulence, chemistry, fuel-surface interaction, and radiative heat transfer is employed to analyze a hydrogen peroxide/HDPE hybrid rocket with swirl injection, whose setup is described in detail in [9]. Such numerical CFD approach is intended as a quick design tool able to aid during the design phase, while at the same time offering useful insights on the physical phenomena taking place inside the engine. Several firing tests are rebuilt, obtaining satisfactory results for both the average regression rate and the chamber pressure, thus validating the numerical approach. Extensive analyses on the most significant features entailed by the swirling motion are carried out, focusing on the swirl decay phenomenon and on the effect of swirl intensity on regression rate and mixing.

The manuscript is organized as follows. The numerical model is presented in Section 2, followed by a brief presentation of the available experimental data (Section 3) and of the computational setup employed in the simulations (Section 4). In Section 5 the results of the simulations are presented.

2. Numerical Model

The numerical simulations have been performed solving the Reynolds-averaged Navier-Stokes equations [15], with submodels accounting for the effects of turbulence, chemistry, gas-surface interaction, and thermal radiation. In all simulations an axisymmetric approach has been used, with a periodic boundary condition on the lateral faces. Such simulations can be used as a quick design tool, while, on the other hand, most of the work present in literature either employs 3D [7, 8] or LES [16] simulations, which have high computational cost. The numerical model is extensively described in [17, 18] and the main details are reported below for the sake of completeness.

The simulations were performed with an in-house solver, validated in many different operating conditions [17, 19, 20, 21]. The model has been successfully applied to swirl injected hybrid rockets at different scales in [22, 23]. The finite-volume computational tool is second-order accurate in time and employs a Roe Riemann solver [24], with the Strang operator-splitting technique used for time integration [25], through a second-order Runge-Kutta scheme for convective and diffusive terms and an implicit integrator for the chemical source terms. The specific isobaric heat, enthalpy and transport properties are expressed, as a function of temperature, using the polynomials taken from the CEA database [26] for all species, and the heats of formation as well. Wilke's rule [15] is used to obtain the mixture molecular transport properties, considering a constant Schmidt number Sc = 0.7. The Prandtl number is computed from the mixture properties. The adopted turbulence model is the one of Spalart-Allmaras [27], with turbulent Prandtl and Schmidt numbers equal to 0.9 and 0.7, respectively. The modeling of turbulence in swirling flows requires particular care, due to the complex vortex structures and the presence of anisotropic characteristics in the turbulent mixing processes. It appears, however, that conventional RANS approaches fail to capture the details of the vortex structure only near the axis [28], thus suggesting how they may be used with good results in the analysis of conventional hybrid rockets, where the fuel grain is wet by the external portion of the vortex.

Table 1: Chemical reactions involved in the global reaction mechanism.

$C_2H_4 + O_2$	$\longrightarrow$	$2\,CO + 2\,H_2$
$C_2H_4 + 2\,H_2O$	$\longrightarrow$	$2\,CO + 4\,H_2$
$CO + H_2O$	$\rightleftharpoons$	$CO_2 + H_2$
$H_2 + \frac{1}{2}\,O_2$	$\rightleftharpoons$	H_2O
O_2	$\rightleftharpoons$	$2\,O$
H_2O	$\rightleftharpoons$	$OH + H$

A global reaction mechanism is employed to model the combustion of ethylene, which is the product of HDPE pyrolysis [29, 30], adapting a model for the combustion of butadiene, due to the lack of literature data, consisting of six reactions and nine species (Table 1) [18]. The forward reaction rates were computed through Arrhenius-type equations and the backward rates as the ratio between the forward ones and the equilibrium constant.

DOI: 10.13009/EUCASS2023-606

At the fuel surface, mass and energy balance equations are solved, in order to evaluate the fuel regression rate. The surface energy balance is written as

$$q_{\text{conv}} + q_{\text{rad}} = \rho_s \dot{r} \left[\Delta h_p + c_s \left(T_w - T_{s,\text{in}} \right) \right] \tag{3}$$

where q_{conv} and q_{rad} are the convective and net radiative heat flux, $\rho_s = 970$ kg/m^3 and $c_s = 1255.2$ J/(kgK) are the fuel density and specific heat, $\Delta h_p = 2.72$ MJ/kg is the fuel heat of pyrolysis, and T_w and $T_{s,\text{in}} = 298.15$ K are the fuel surface temperature and the fuel initial temperature. The surface mass balance for each species is instead

$$\rho D_{im} \frac{\partial y_i}{\partial \eta} + \dot{\omega}_i = (\rho_s \dot{r}) y_i \quad i = 1, .., 9 \tag{4}$$

where D_{im} is the i^{th} species-to-mixture effective diffusion coefficient, y_i the gas phase mass fraction of the i^{th} species at the wall, $\dot{\omega}_i$ the rate of production of gas-phase species i due to fuel pyrolisis, and η is the coordinate normal to the fuel surface. HDPE pyrolysis is modeled through an Arrhenius-type law,

$$\dot{r} = A \exp(-E_a/(2RT_w)) \tag{5}$$

where the pre-exponential constant is $A = 4.78 \times 10^{-3}$ m/s, the activation energy is $E_a = 251.04$ kJ/mol, and R is the universal gas constant. The values for A and E_a, and also the fuel heat of pyrolisis and specific heat, are taken from [31]. The fuel density was instead experimentally measured. Coupled solution of Eqs. (3), (4) and (5) with a Newton-Raphson method allows to evaluate the wall temperature and composition, and the fuel regression rate.

The radiative heat flux is computed with an in-house code [17, 32], which integrates the radiative heat transfer equations (RTE) [33] for gray/diffuse boundaries and inhomogeneous gray/nonscattering media, using the discrete transfer method [34], in which a discretization of N_r rays is used to integrate the RTE with an integration step Δs. The evaluation of the radiative heat flux is carried out only at the boundaries and the sole emitting species considered are H_2O, CO_2 and CO, with their mean Planck absorption coefficients taken from [35]. The wall emissivity is set to 0.91. For all simulations $N_r = 244$ rays with an integration step of $\Delta s = 0.5$ mm have been used.

3. Experimental Data

In this section the experimental data employed for the numerical rebuilding are briefly reported. The interested reader is referred to [9] for further details. Three different injection plates are used, each with a different SN_g (Tab. 2). For each injection plate, a different grain length (L_{grain}) is employed, in order to have similar oxidizer to fuel ratios (O/F) for all tests. In order to maximize the engine performance, the design mixture ratio is 6. For each injection plate, tests are performed with different post-chamber lengths (L_{post}) and average port radii ($r_{p,\text{ave}}$). The employed oxidizer mass flow rate is 100 g/s for all tests and the hydrogen peroxide concentration is 91.5%. Each configuration is characterized by the employed injector (Fig. 1), the postchamber length, and the initial grain port diameter, which are all reported in the test name. The initial port diameter is expressed by the notation _10 or _20, which indicates that the initial grain port is equal to the estimated grain port after 10 or 20 s of burning time with respect to the initial configuration (stopped and restarted burn).

Table 2: Experimental data.

	Test	SN_g	L_{grain} (mm)	L_{post} (mm)	$r_{p,\text{ave}}$ (mm)	$\dot{r}_{\text{for}}$ (mm/s)	$\dot{r}_{cen}$ (mm/s)	p_{cc} (bar)
●	D5N10PC20	2	170	20	16.75	1.12	0.88	20.05
■	D5N10PC50	2	170	50	16.95	1.12	0.84	21.44
◆	D5N10PC50_10	2	170	50	24.18	0.66	0.55	20.61
▲	D5N10PC50_20	2	170	50	30.15	0.49	0.51	20.18
●	D4.5N10PC20	2.53	140	20	16.25	1.19	0.77	20.82
■	D4.5N10PC35	2.53	140	35	16.17	0.95	0.79	20.29
◆	D4.5N10PC50	2.53	140	50	16.81	1.04	0.81	20.71
▲	D4.5N10PC50_10	2.53	140	50	26.09	0.55	0.57	18.82
●	D5N6PC20	3.33	125	20	17.23	1.37	0.84	21.08
■	D5N6PC35	3.33	125	35	17.58	1.61	0.94	21.09
◆	D5N6PC50	3.33	125	50	17.73	1.82	0.90	20.98
▲	D5N6PC50_10	3.33	125	50	27.89	0.62	0.62	20.58

DOI: 10.13009/EUCASS2023-606

If not specified, the initial port diameter is equal to the prechamber diameter. The injector name specifies the number and diameter of injector holes (for example, D5N10 means 10 holes of 5 mm diameter each). The length of the postchamber is reported in millimiters in the test name (for example PC20 means $L_{\text{post}} = 20$ mm). For the regression rate analysis, the final grain profile has been approximated with the two-cylinder model of Fig. 2, in order to take into account the fact that the forward section of the fuel grain (approximately the first 10%) showed a higher regression rate ($\dot{r}_{\text{for}}$) than the central portion of the grain ($\dot{r}_{cen}$).

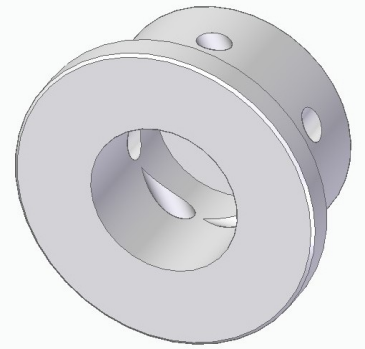

Figure 1: D5N6 vortex injector.

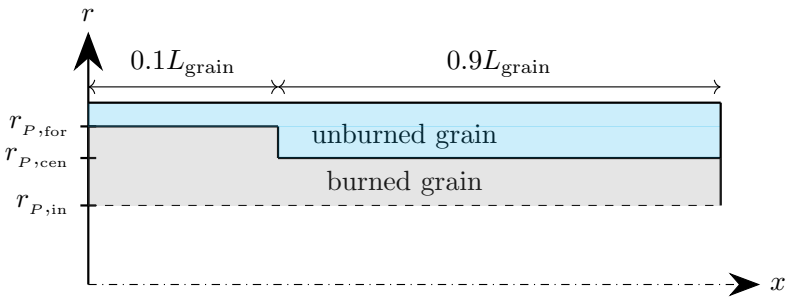

Figure 2: Representation of the grain internal volume model employed for the regression rate analysis. The dashed line is initial grain shape, the solid line the final grain profile.

4. Computational Setup

In this section, the different computational setups employed for the numerical simulations are described. The main computational setup employed in the simulations (Fig. 3) is based on the experimental apparatus described in [9]. It consists of a prechamber ($0 < x < x_2$, $L_{\text{pre}} = x_2$), a fuel grain ($x_2 < x < x_3$, $L_{\text{grain}} = x_3 - x_2$), a postchamber ($x_3 < x < x_4$, $L_{\text{post}} = x_4 - x_3$), and a converging-diverging nozzle ($x_4 < x < L$). The prechamber hosts a swirl injector ($x_0 < x < x_1$), through which the products of H_2O_2 dissociation, computed through CEA under the equilibrium hypothesis, are injected. The mass fractions of the dissociation products are 0.57 and 0.43 for H_2O and O_2 respectively, and the injection temperature is 1066 K. On the remaining walls of the prechamber, an adiabatic boundary condition is set. The nozzle is composed by conical sections connected by circular arcs with each other and with the postchamber. The postchamber radius has been taken equal to the fuel grain radius r_{p}, since previous studies [21, 23] have shown that the modeling of the postchamber cavity has limited effects on the chamber pressure and almost no effect on the fuel regression rate.

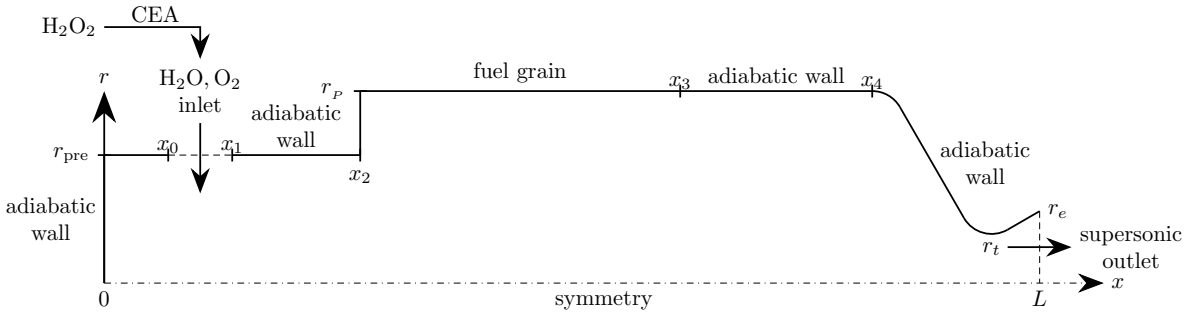

Figure 3: Computational setup.

The three-dimensional swirl injector (Fig. 1), which is composed by several channels feeding the oxidizer tangentially inside the engine, is here modeled as an annular injector, due to the axisymmetric flow assumption. This simplification is considered acceptable since it is deemed that the three-dimensional effects are confined near the injector and have only limited effects on the fuel grain regression. The annulus width is set to match the injection area

DOI: 10.13009/EUCASS2023-606

of the reference injector and the injection angle of the flow is set to match the desired geometric swirl number. In order to impose a certain geometric swirl number at the injection, a rewriting of Eq. (1) is needed, in order to link the swirl number and the geometrical characteristics of the axisymmetric injector, namely the wall radius, the annulus width, and the injection angle. Applying the conservation of mass flow rate and angular momentum, under the hypothesis of inviscid and isothermal flow, and of uniform axial velocity (at a certain distance from the injector), one obtains the following equation

$$SN_g = \frac{r_{\text{pre}}}{2(x_1 - x_0)} \tan(\beta) \tag{6}$$

For the sake of simplicity, the same annular injector has been used to simulate all three vortex injectors, varying only the angle β to achieve the desired SN_g. It is in fact assumed that the other details of the injection have only second-order effects on the parameters of interest of the engine.

The prechamber dimensions are: $x_0 = 9.75$ mm, $x_1 = 11.25$ mm, $x_2 = 27$ mm, and $r_{\text{pre}} = 12.5$ mm. The port radius r_p, fuel length L_{grain} and postchamber length L_{post} depend on the simulated test (see Tab. 2), while the throat radius is $r_t = 5.45$ mm for all configurations. The computational grid is made of three structured blocks, the first for the injector and other two for the fuel grain, postchamber, and nozzle. For the D5N6PC20 case, reported in Fig. 4, the blocks are composed of 60×40 (block 1), 136×40 (block 2), and 136×60 (block 3) cells respectively.

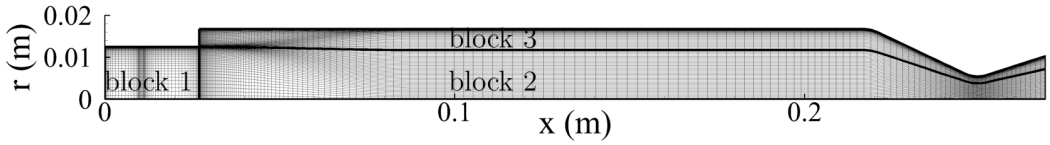

Figure 4: Computational grid for the D5N6PC20 test.

A different computational setup was employed to perform simulations of the injectors alone. It consists only of the prechamber ($0 < x < x_2$) with the swirl injector ($x_0 < x < x_1$). Adiabatic boundary conditions are set on all walls and a subsonic outlet condition (imposed pressure) has been set on the exit section. When simulating the sole injector the prechamber length has been increased to 100 mm.

5. Numerical results

In this section, the results obtained from the CFD simulations are reported and analyzed. First, in Section 5.1, the results of the simulations of the vortex injectors are presented, then in Section 5.2 a comparison of the full-engine simulations with the experimental data is performed, focusing on the peculiar characteristics of the flowfield entailed by the swirl injection.

5.1 Injector head simulations

Being the numerical approach adopted in this work based on axisymmetric simulations, a simplified modeling strategy for the injector head had to be employed, modeling the vortex injector with an equivalent annular axisymmetric injector. To verify whether the application of Eq. (6) leads to a reasonable evaluation of the swirl number, in the limits of the simplifying assumptions, three simulations were performed, one for each injector, in order to compare the imposed SN_g and the resulting SN. To do so a computational setup consisting of the sole injector was employed, with an extended prechamber length in order to ensure a complete development of the flow. The pressure at the outlet was set to 20 bar for all simulations and the mass flow rate was the same of the experimental tests.

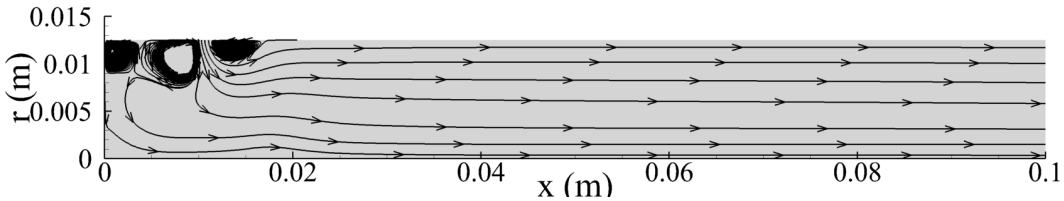

Figure 5: Streamlines for the D5N6 injector.

DOI: 10.13009/EUCASS2023-606

Fig. 5 shows the streamlines for the D5N6 injector head (no significant change is present changing SN_g). Several recirculation zones are formed near the wall, as expected, with another one starting to form near the motor axis, due to the centrifugal effects pushing the flow away from the centerline.

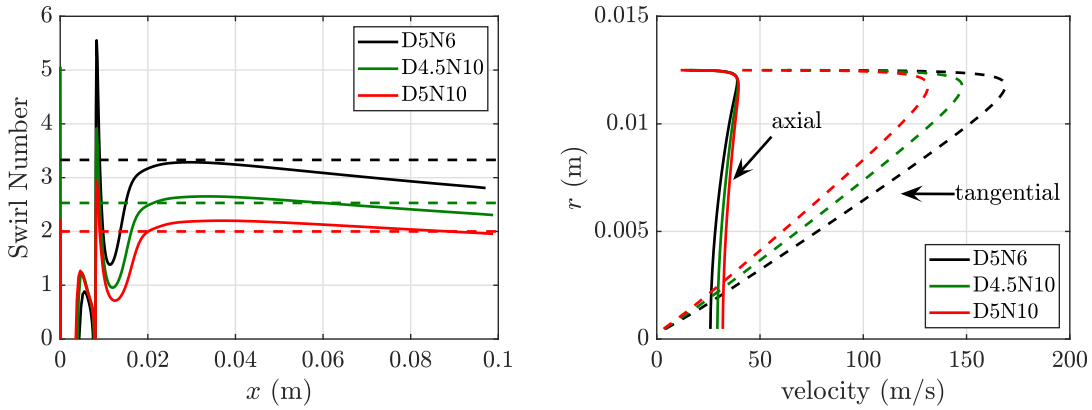

(a) Swirl number evolution for the three simulated injectors.

(b) Velocity profiles at $x = 0.08$ m.

Figure 6: Effect of swirl intensity on swirl number and flow velocity.

The swirl numbers computed applying the definition (Eq. (1)) are reported in Fig. 6(a) for all injectors. It can be seen that a quite complex zone is present before the end of the injector ($x \approx 0.01$ m), with a sudden increase, a maximum and then a slow decrease. The maximum is due the effective cross-section of the flow increasing up to $x \approx 0.02$ m, because the recirculation zones have zero net axial flow and thus lead to an increase of the denominator of Eq. (1). After the flow has cleared all the recirculation zones, the viscous decay phenomena lead to a slow decay of the swirl intensity [11]. It can be seen that for the D5N10 and D4.5N10 injectors the computed swirl number is higher than SN_g, while for the D5N6 injector the two values are almost equal. This effect is likely due to the non-uniformity of flow properties, which was assumed in the derivation of Eq. (6). As shown in Fig. 6(b), the flow reaches a forced-vortex structure (almost linear increase of tangential velocity with the radius), with a non-uniform axial velocity. Nonetheless, given also the results of the rebuilding presented in the following section, it is deemed that the adopted modeling technique is able to correctly reproduce the main features of the flow field induced by a swirl injector. Furthermore, the forced-vortex profile is in accordance with experimental results [36] and three-dimensional simulations [8] that have been performed on similar swirl injectors.

5.2 Full engine simulations

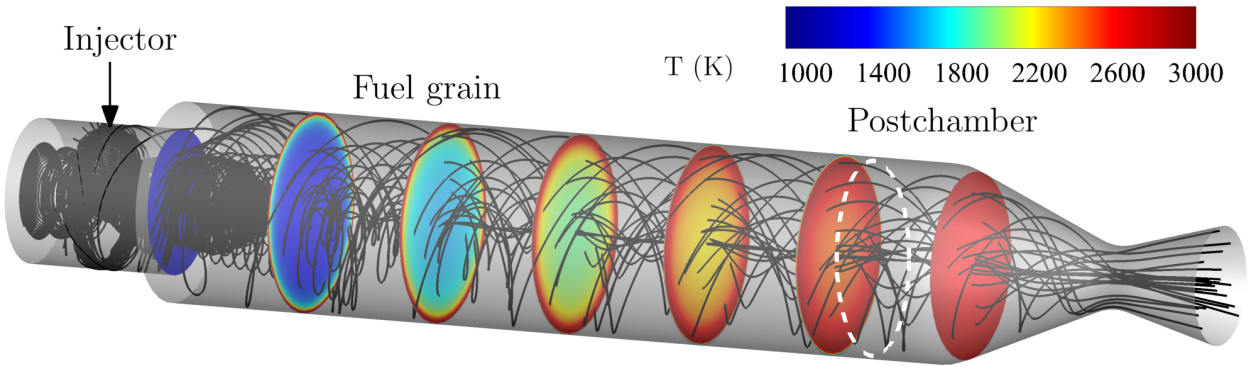

Figure 7: Three-dimensional streamlines and temperature field for the D5N6PC20 test case. The dashed white line marks the start of the postchamber.

In this section the results of the simulations performed on the full engine setup are reported. For each of the tests reported in Tab. 2 a simulation has been performed at the average port diameter.

DOI: 10.13009/EUCASS2023-606

The flowfield, which is qualitatively similar for all test cases, is shown in Fig. 7 for the D5N6PC20 test. The three-dimensional representation has been obtained rotating the axisymmetric solution around the motor axis. Besides the recirculation zones close to the injector, present also in the simulations of the sole injector head, a large vortex is formed near the axis at the prechamber-grain transition, where the swirling flow is pushed towards the grain by the strong centrifugal forces, leading to the development of a thin flame quite close to the fuel grain. The flame then slowly widens until a quite good mixing is reached in the postchamber. From Fig. 7 one can also identify the progressive decay of the swirling motion and the straightening of the streamlines, especially in the postchamber and in the nozzle. This is due to the increase in the axial component of velocity, due to the mixing and temperature rise in the postchamber and to the cross-section variation in the nozzle.

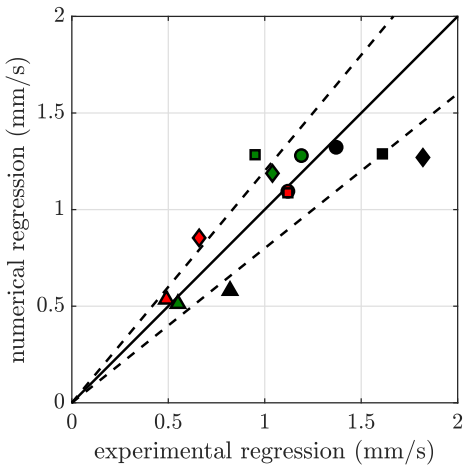

(a) Regression rate in the forward section of the grain.

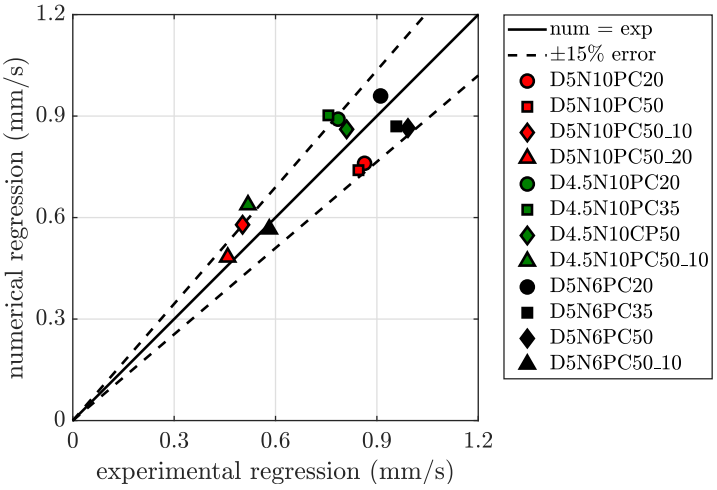

(b) Average regression rate.

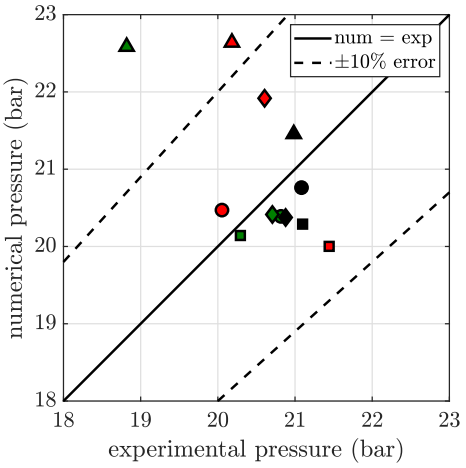

(c) Wall pressure at postchamber end.

Figure 8: Experimental rebuilding.

An extensive comparison with the experimental data is reported in Fig. 8. The average numerical and experimental regression rates compare reasonably well for all simulated tests, showing a fairly good agreement (Fig. 8(b)). It is interesting to note that the regression rate of the D4.5N10 tests is always overestimated, while for the D5N10 injector it is underestimated at small port radii and slightly overestimated at large port radii. No appreciable trend can be instead identified for the D5N6 injector head. For what concerns the regression rate in the forward section of the grain, Fig. 8(a) shows that the agreement is worse than the one obtained with the average regression. This is reasonable, since the adopted modeling strategy is not able to capture the grain shape change over time, which can have a deep influence on the observed regression rate peak. For what concerns the chamber pressure rebuilding (Fig. 8(c)), a satisfactory

DOI: 10.13009/EUCASS2023-606

agreement is obtained, with an error less than 5% for most test cases.

The comparison between numerical and experimental results shows no clear trend, with the simulations either overestimating or underestimating the regression rate and the chamber pressure depending on the swirl number and the port radius. For the D4.5N10 injector, results suggest that a systematic error may be present, such as an overestimation of the swirl number with respect to the experimental configuration.

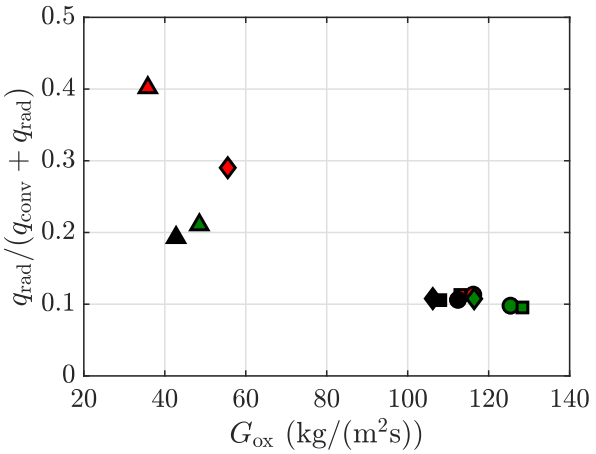

Figure 9: Radiative heat flux share.

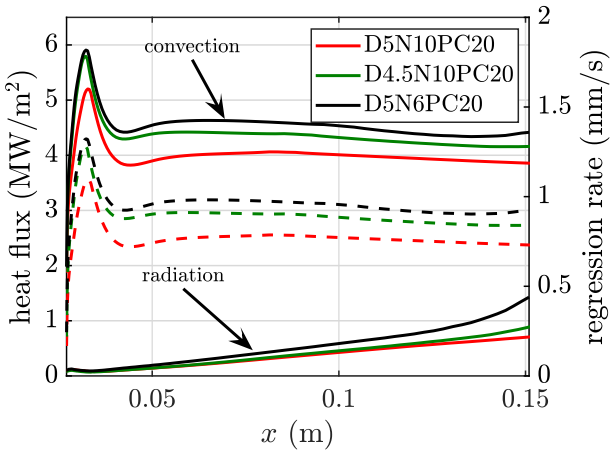

Figure 10: Heat flux (solid lines) and regression rate (dashed lines) for the PC20 tests.

Fig. 9 shows the radiative heat flux share for the simulated tests versus the oxidizer mass flux (G_{ox}). At low port diameters (high mass flux) radiation accounts only for the 10% of the overall heat flux, while the radiative heat share increases at high port diameters, due to the increase in the emitted radiation (the hot gas volume is larger) and the reduced convection due to the lower mass flux.

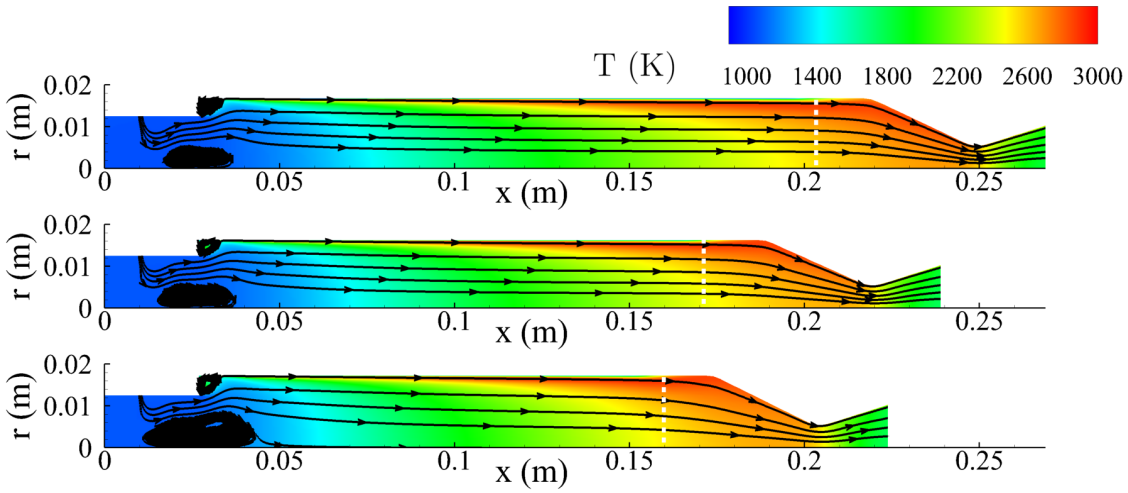

Figure 11: Temperature contours with streamlines for D5N10PC20 (top), D4.5N10PC20 (middle) and D5N6PC20 (bottom) tests. The white dashed line marks the start of the postchamber.

It is interesting to analyze the heat flux and regression rate profiles, reported in Fig. 10 for the PC20 tests. Increasing the swirl number both radiation and convection increase, the former due to the slightly larger flame (due to the increased mixing) and the latter due to the increased flow velocity. While the radiative heat flux increases monotonically along the grain, due to the monotone axial increase of the flame thickness, the convective heat flux shows a peak and a subsequent plateau. The initial peak in convection is due to the presence of the recirculation zone, which reduces the effective cross-section and leads to an increase in the local mass flux and thus in heat transfer. Being

DOI: 10.13009/EUCASS2023-606

the radiative heat flux quite small, especially at the start of the grain, the regression rate profile closely follows the one of the convective heat flux.

The temperature contours at various swirl numbers, for the same postchamber length, are reported in Fig. 11. It can be seen that the recirculation zone near the axis increases in size with SN_g, due to the augmented centrifugal forces, and that the flowfields are qualitatively similar for all three cases.

Some of the characteristics of the vortex flow evolution along the engine are reported in Figs. 12 and 13. As expected, the vortex induced by the injector follows closely a forced vortex profile (up to the boundary layer edge), with the maximum tangential velocity decreasing due to viscous decay and the axial velocity increasing due to mass adduction and energy release. This results in a strong decay of the swirl number along the engine, which leads to quite similar SN values at the end of the postchamber for all three injectors. The strong decay that can be seen in the final part of the engine is due to the strong flow acceleration in the nozzle.

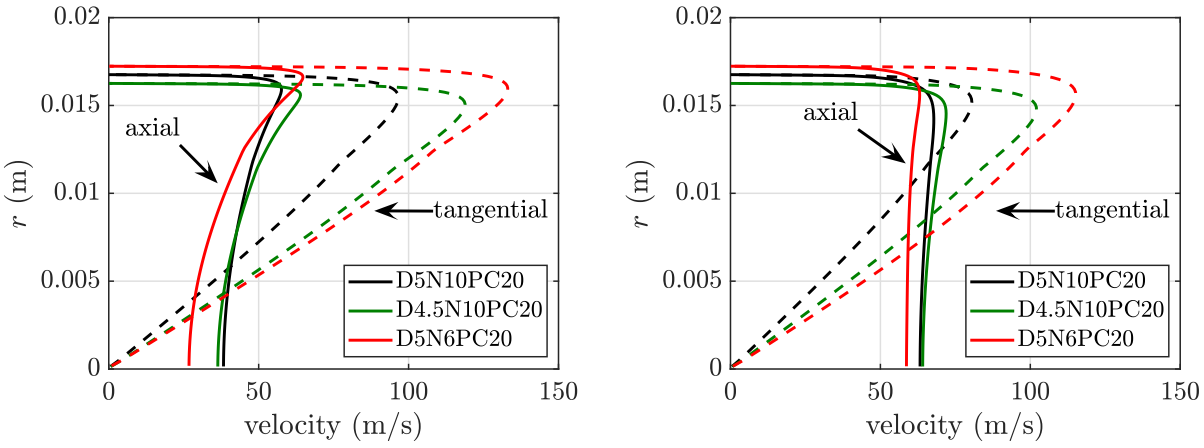

(a) Middle grain.

(b) Grain end.

Figure 12: Velocity profiles. Solid lines: axial component; dashed lines: tangential component.

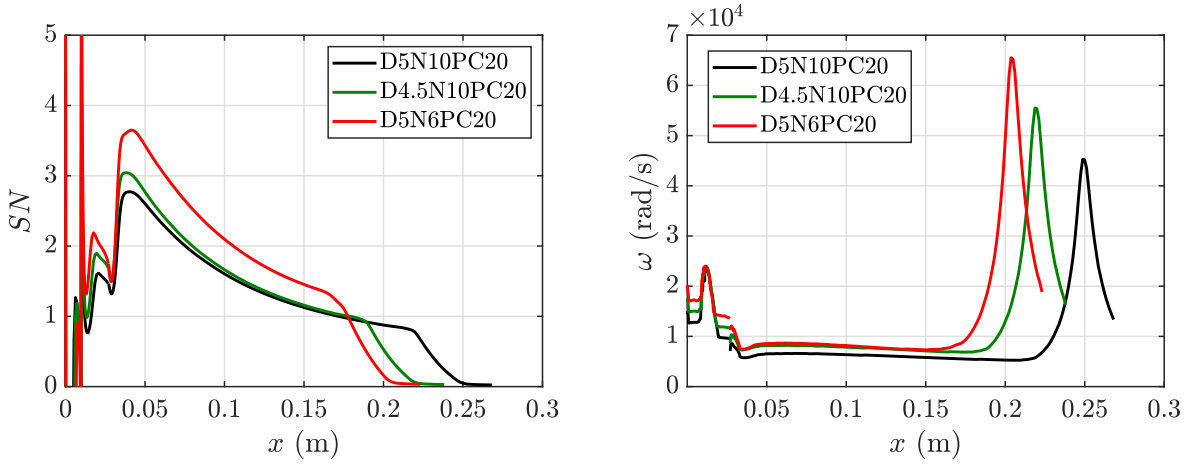

(a) Swirl number.

(b) Angular velocity.

Figure 13: Swirl decay along the engine.

Another interesting parameter is the angular velocity of the vortex, computed as the ratio between the maximum tangential velocity and the radius were it occurs for each section. It decreases sharply at the prechamber-grain transition, decays slowly along the engine and then has a peak at the nozzle throat. In fact, applying the conservation of angular momentum, and assuming that the velocity profile $w = \omega r$ is the same for all sections, one obtains that $\omega = \omega_0 (r_0/r)^2$, where ω_0 and r_0 are a reference angular velocity and radius. A similar reasoning can be applied to the swirl number, which is approximately $SN \approx w/u$. Since the axial component of velocity varies with the cross-section (and thus $\propto r^2$)

DOI: 10.13009/EUCASS2023-606

and the tangential velocity as $\omega r \propto 1/r$, one obtains that the swirl number variation with the wall radius is linear, provided that one uses always the same value to make Eq. (1) non-dimensional. Finally, looking at Figs. 12 and 13, we note that the strong swirl decay is mainly due to the axial acceleration of the flow rather than to the decay of the rotational component of velocity.

Fig. 14 shows the temperature contours for the D4.5N10 injector head, at different postchamber lengths. It can be seen that a relatively good mixing can be obtained even with the small prechamber, thanks to the swirling flow. An improvement can however be reached increasing the postchamber length to 50 mm. In fact, as reported in Fig. 15, the mixture at the nozzle entrance section is much more homogeneous, both in terms of temperature and composition, increasing the postchamber length.

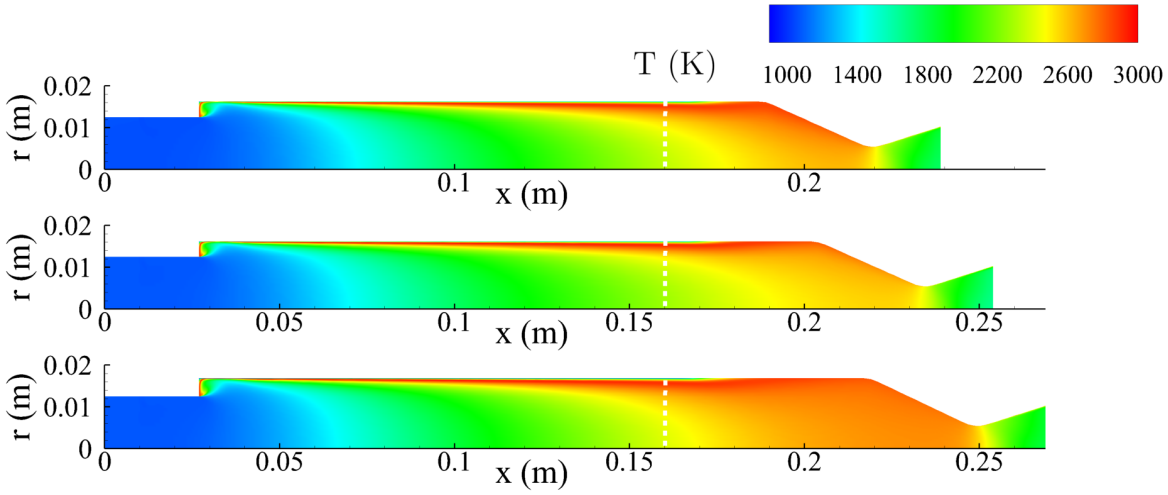

Figure 14: Temperature contours for D4.5N6PC20 (top), D4.5N6PC35 (middle) and D4.5N6PC50 (bottom) tests. The dashed white line marks the start of the postchamber.

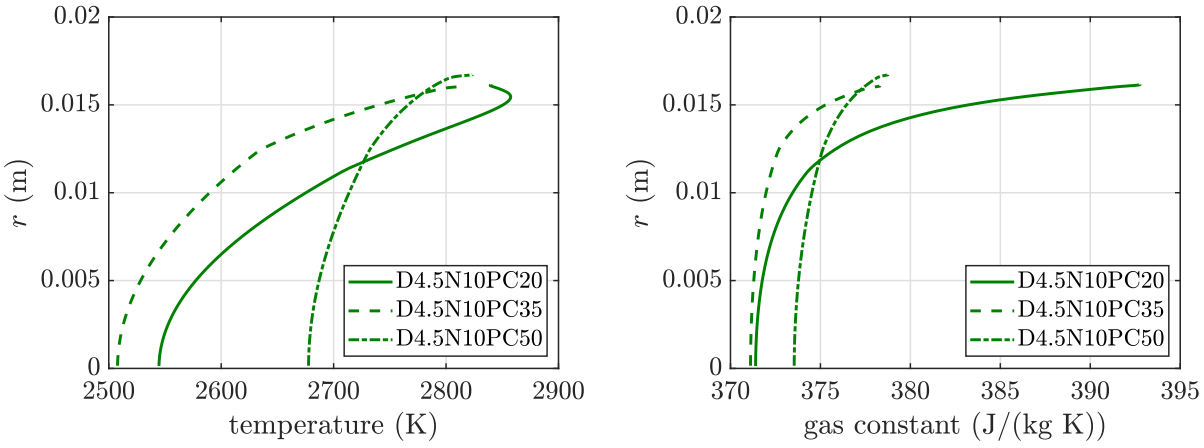

(a) Temperature.

(b) Gas constant.

Figure 15: Effect of postchamber length on mixing.

DOI: 10.13009/EUCASS2023-606

6. Conclusions

In this work numerical simulations of a swirl-injected hybrid rocket burning hydrogen peroxide and high-density polyethylene have been performed. Twelve test cases, with different geometric swirl numbers, average port diameters, and postchamber lengths have been rebuilt performing a simulation at the test average diameter. The resulting regression rate and chamber pressure compare with fairly good agreement (±15% error) with the experimental results. This is regarded as acceptable considering the adopted simplifying hypotheses and the fact that a single constant-diameter simulation may not be able to capture the details of the grain evolution over time.

The simulations show that, at the simulated port diameters and swirl numbers, the regression rate is mainly due to convection, with radiation accounting for up to 30/40% of the total wall heat flux only for a few tests. The predicted regression rate profile is in accordance with the experimental data, which show a higher regression rate in the forward section of the fuel grain. An analysis has been performed also on the swirl decay phenomenon along the engine, which appears to be driven mainly by the increase in axial component of velocity due to mass adduction, combustion, and cross-section variation, while the decrease in tangential velocity due to friction has only a second-order effect.

References

[1] M. J. Chiaverini, N. Serin, D. K. Johnson, Y.-C. Lu, K. K. Kuo, and G. A. Risha. Regression rate behavior of hybrid rocket solid fuels. *Journal of Propulsion and Power*, 16(1):125–132, 2000.

[2] D. Altman and A. Holzman. Overview and history of hybrid rocket propulsion. In K. K. Kuo and M. J. Chiaverini, editors, *Fundamentals of Hybrid Rocket Combustion and Propulsion*, volume 218 of *Progress in Astronautics and Aeronautics*, pages 1–36. AIAA, Reston, VA, 2007.

[3] D. Pastrone. Approaches to low fuel regression rate in hybrid rocket engines. *International Journal of Aerospace Engineering*, 2012, 2012.

[4] A. K. Gupta, D. G. Lilley, and N. Syred. *Swirl flows*. Abacus Press, 1984.

[5] R. F. Lopina and A. E. Bergles. Heat transfer and pressure drop in tape-generated swirl flow of single-phase water. *Journal of Heat Transfer*, 91(3):434–441, 1969.

[6] T. Takashi, S. Yuasa, and K. Yamamoto. Effects of swirling oxidizer flow on fuel regression rate of hybrid rockets. *35th Joint Propulsion Conference and Exhibit*, 1999.

[7] N. Bellomo, F. Barato, M. Faenza, M. Lazzarin, A. Bettella, and D. Pavarin. Numerical and experimental investigation of unidirectional vortex injection in hybrid rocket engines. *Journal of Propulsion and Power*, 29(5):1097–1113, 2013.

[8] E. Paccagnella, F. Barato, D. Pavarin, and A. Karabeyolu. Scaling parameters of swirling oxidizer injection in hybrid rocket motors. *Journal of Propulsion and Power*, 33(6):1378–1394, 2017.

[9] M. Franco, F. Barato, E. Paccagnella, M. Santi, A. Battiston, A. Comazzetto, and D. Pavarin. Regression rate design tailoring through vortex injection in hybrid rocket motors. *Journal of Spacecraft and Rockets*, 57(2):278–290, 2020.

[10] C. Palani Kumar and A. Kumar. Effect of swirl on the regression rate in hybrid rocket motors. *Aerospace Science and Technology*, 29, 2013.

[11] F. Chang and V.K. Dhir. Turbulent flow field in tangentially injected swirl flows in tubes. *International Journal of Heat and Fluid Flow*, 15(5), 1994.

[12] K. Ozawa and T. Shimada. Linear combustion stability analysis of uni-directional vortex injection hybrid rocket engines. *50th AIAA/ASME/SAE/ASEE Joint Propulsion Conference*, 2014.

[13] T.C. Claypole and N. Syred. The effect of swirl burner aerodynamics on NOx formation. *18th Symposium (International) on Combustion*, 1981.

[14] N. Syred and J.M. Beér. Combustion in swirling flows: A review. *Combustion and Flame*, 23(2), 1974.

[15] J. D. Anderson. *Hypersonic and High-Temperature Gas Dynamics*. AIAA Education Series, 2006.

DOI: 10.13009/EUCASS2023-606

[16] M. Motoe and T. Shimada. Numerical simulations of combustive flows in a swirling-oxidizer-flow-type hybrid rocket. *52nd Aerospace Sciences Meeting*, 2014.

[17] M. T. Migliorino, D. Bianchi, and F. Nasuti. Numerical analysis of paraffin-wax/oxygen hybrid rocket engines. *Journal of Propulsion and Power*, 36(6):806–819, 2020.

[18] D. Bianchi, G. Leccese, F. Nasuti, M. Onofri, and C. Carmicino. Modeling of High Density Polyethylene Regression Rate in the Simulation of Hybrid Rocket Flowfields. *Aerospace*, 6(8), 2019.

[19] M. T. Migliorino, D. Bianchi, and F. Nasuti. Numerical Simulations of the Internal Ballistics of Paraffin-Oxygen Hybrid Rockets at Different Scales. *Aerospace*, 8(8), 2021.

[20] D. Bianchi, B. Betti, F. Nasuti, and C. Carmicino. Simulation of Gaseous Oxygen/Hydroxyl-Terminated Polybutadiene Hybrid Rocket Flowfields and Comparison with Experiments. *Journal of Propulsion and Power*, 31(3):919–929, 2015.

[21] M. T. Migliorino, G. Gubernari, D. Bianchi, F. Nasuti, D. Cardillo, and F. Battista. Numerical Simulations of Fuel Shape Change in Paraffin-Oxygen Hybrid Rocket Engines. *Journal of Propulsion and Power*, published online(article in advance):1–15, 2023.

[22] M. T. Migliorino, M. Fabiani, C. Paravan, D. Bianchi, F. Nasuti, L. Galfetti, R. C. Pellegrini, and E. Cavallini. Numerical and experimental investigation of a lab-scale paraffin motor with swirled injection of gaseous oxygen. *9th European Conference for Aeronautics and Aerospace Sciences (EUCASS)*, 2022.

[23] M. T. Migliorino, M. Fabiani, D. Bianchi, F. Nasuti, F. Barato, N. Bellomo, D. Pavarin, S. Pizzurro, M. Pizzarelli, R. C. Pellegrini, and E. Cavallini. Numerical simulations of a paraffin-hydrogen peroxide hybrid rocket with swirl injection. *AIAA Scitech 2023*, 2023.

[24] P.L Roe. Approximate riemann solvers, parameter vectors, and difference schemes. *Journal of Computational Physics*, 43(2):357–372, 1981.

[25] G. Strang. On the construction and comparison of difference schemes. *SIAM Journal on Numerical Analysis*, 5(3):506–517, 1968.

[26] B. J. McBride, M. J. Zehe, and S Gordon. NASA Glenn coefficients for calculating thermodynamic properties of individual species. *NASA TP-2002-211556*, 2002.

[27] P. Spalart and S. Allmaras. A one-equation turbulence model for aerodynamic flows. *AIAA*, 439, 1992.

[28] F. Barato, E. Paccagnella, G. Venturelli, D Pavarin, F. Picano, and J-Y. Lestrade. Numerical simulations of an isochoric hybrid rocket combustion chamber and comparison with tests. *8th European Conference for Aeronautics and Aerospace Sciences (EUCASS)*, 2019.

[29] B. M. Fabuss, J. O. Smith, R. I. Lait, A. S. Borsanyi, and C. N. Satterfield. Rapid thermal cracking of n-hexadecane at elevated pressures. *Ind. Eng. Chem. Proc. Des. Dev.*, 1(4):293–299, 1962.

[30] B. Blouri, F. Hamdan, and D. Herault. Mild cracking of high-molecular-weight hydrocarbons. *Ind. Eng. Chem. Proc. Des. Dev.*, 24(1):30–37, 1985.

[31] G. Lengelle, B. Fourest, J. Godon, and C. Guin. Condensed-phase behavior and ablation rate of fuels for hybrid propulsion. *29th Joint Propulsion Conference and Exhibit*, 1993.

[32] G. Leccese, D. Bianchi, B. Betti, D. Lentini, and F. Nasuti. Convective and radiative wall heat transfer in liquid rocket thrust chambers. *Journal of Propulsion and Power*, 34(2):318–326, 2018.

[33] M. F. Modest and S. Mazumder. *Radiative Heat Transfer*. Academic Press, 4th edition, 2022.

[34] F.C. Lockwood and N.G.Shah. A new radiation solution method for incorporation in general combustion prediction procedures. *18th Symposium (International) on Combustion*, 1981.

[35] P. Rivière and A. Soufiani. Updated band model parameters for h_2o, co_2, ch_4 and co radiation at high temperature. *International Journal of Heat and Mass Transfer*, 55(13):3349–3358, 2012.

[36] F. Chang and V.K. Dhir. Mechanisms of heat transfer enhancement and slow decay of swirl in tubes using tangential injection. *International Journal of Heat and Fluid Flow*, 16(2), 1995.